Technische Universität München
Fakultät für Physik

Abschlussarbeit im Bachelorstudiengang Physik

Study of the photon identification in pp at $\sqrt{s} = 13$ TeV in ALICE for the Σ^0 reconstruction

Maximilian Korwieser

29. September 2018

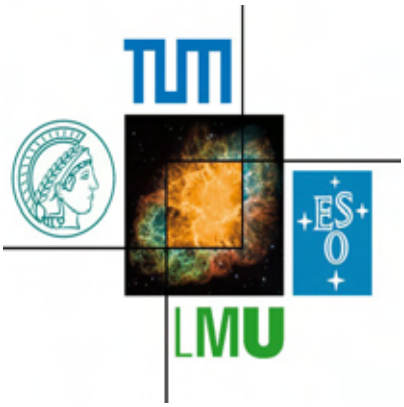

Erstgutachter (Themensteller): Prof. L. Fabbietti
Zweitgutachter: Prof. X. XXXX

Betreuer: M.Sc A. Mathis

Contents

Abstract

The decay of Σ^0 produces Λ and a low energy photon which can only be detected indirectly by the ALICE detector via the conversion into an e^+e^- pair. With the help of Monte Carlo (MC) simulations the characteristic features of the photon were examined. This enabled the fine tuning of the selection criteria in order to maximize the reconstruction efficiency of the photon, thus improving the yield of Σ^0. For the analysis, pass 1 data in the ESD format, gathered from 2016 and 2017 in pp collisions is used. With in total 1.04×10^9 minimum bias events. The total yield of $(\Sigma^0 \oplus \overline{\Sigma^0})$ was determined to be (24989 $\pm$ 317). Additionally, the efficiency for $(\Sigma^0 \oplus \overline{\Sigma^0})$ was determined with the help of the generated MC sample and the value of the p_{T} averaged purity was calculated to be 26.4 %. The efficiency provided important information for the correction of the measured p_{T} spectra. Sharing its quark contents with the Λ hyperon, Σ^0 also shares physical properties such as charge and the third component of the isospin I_3 with Λ. Both particles differ in their mass with a difference of about 76 MeV and in their total isospin I, which is 1 for Σ^0 and 0 for Λ, making them isospin partners. The extraction of the ratio Σ^0/Λ is therefore crucial in determining possible differences in the production mechanisms and provides thus insights in the baryon production. The result of the ratio Σ^0/Λ was found to be (0.219 $\pm$ 0.005) and is in the same order of magnitude as the prediction of 1/3 from theory. The deviation of the obtained ratio for Σ^0/Λ from the value predicted by theory is subject of further investigation, including a detailed analysis of systematic uncertainties.

Chapter 1

Introduction

1.1 Study of asymptotically free QCD matter

As all known hadrons are bound states of quarks the profound study of these fundamental "building block" particles is of utmost interest in order to understand the physics dominant on smaller scales than on the order of 1 fm. However, this is a difficult task because of the observed running of the quantum chromodynamic (QCD) coupling constant α_s, which is shown in Fig. 1.1. For interactions between quarks with high virtuality, meaning large energy scales Q, the value of α_s is decreasing, leading to asymptotically free quarks. On the other hand, for low virtuality with small Q the increase of α_s is very steep and confines the quarks by strongly binding them to each other. This is the reason why no quarks can be observed outside of bound states, such as hadrons. In order to have access to essentially asymptotic free quarks processes in which very large momenta are transferred have to be studied where α_s is negligible. This is achieved by ultra-relativistic collider experiments at the Large Hadron Collider (LHC) at the European Organization for Nuclear Research (CERN[1]) located in Geneva. By providing center-of-mass energies up to $\sqrt{s} = 13$ TeV for different collision systems (proton-proton [pp], proton-lead [p-Pb] or lead-lead [Pb-Pb]) inelastic scatterings involving large Q are observed and studied. In combination with sophisticated detectors providing the necessary precise particle identification (PID) capabilities the phase diagram of QCD matter is explored, as shown in Fig. 1.2. One of the most prominent predictions of QCD matter is a phase transition from hadronic matter to a new state of matter called Quark Gluon Plasma (QGP) at large temperatures and/or densities. The LHC enables to scan high temperatures T with low values for the chemical potential of baryons μ_B. This produces conditions which may lead, in the case of heavy ion (HI) collisions, to the formation of the QGP. The most defining aspect of the QGP is the fact that inside its volume all quarks and gluons are locally deconfined. This introduces new degrees of freedom depending on the flavour, colour, spin degeneracy and charge, which inevitable leads to a high density of colour fields. This environment allows to employ the grand canonical ensemble (GCE) known from thermo dynamics, in

[1] Conseil européen pour la recherche nucléaire

order to describe the system. Although every quantum number has to be conserved system-wide in the GCE the conservation can locally be broken, leading to effects characteristic for QGPs. In this case, the QGP behaves effectively not only as heat bath but also as reservoir for strangeness for smaller portions of the system thus allowing for a rapid local production of s and $\overline{s}$. The rapid production is necessary because the time available to produce the strangeness abundance is on the order of the collision time scale of 10^{-23} s [3]. The by far largest contribution to the production of strangeness is due to the gluon-gluon (gg) fusion mode $gg \rightarrow s\overline{s}$, which becomes accessible in the deconfined medium. The gg fusion mode is independent from the details of the QGPs formation, and hence insensitive to the initial state. This effect, leading to higher yields of hyperons[2] during the hadronization process, is the so called strangeness enhancement. Observations of strangeness enhancement exist for a variety of hadrons containing strangeness such as Λ and Ξ^-, as shown in Fig. 1.3. The enhancement is more pronounced with increasing multiplicity, which is a measure for the energy and centrality of the HI collision. The same is true for high multiplicity pp collisions where a strangeness enhancement is seen with respect to minimum bias events. Intriguing is the smooth evolution of the enhancement with multiplicity, independently of the collision systems[3]. One hypothesis is that small droplets of QCP are formed, however as by now no experimental data is available to verify this hypothesis, the mechanism is subject to further investigation [4]. A comprehensive way of arranging baryons, which are bound states of three quarks, is realized with the baryon octet shown in Fig. 1.4. The baryon octet is a graphical representation of the Gell-Mann-Nishijima formula,

$$Q = I_3 + \frac{B+S}{2} \ . \tag{1.1}$$

Each solution to this formula corresponds to a baryon, with the third component of the isospin I_3, baryon number B, strangeness S and electromagnetic charge Q. Two strangeless combinations of quarks are included in the octet. These two are composite particles of light flavoured (u, d) quarks therefore they should have similar masses. The electromagnetic charge of the particle depends on the quark content, hence the combination (uud) carries a charge of $+1$ and correspondingly (uud) of 0. As a result, the quark combination (uud) is attributed to the proton, while the counterpart (udd) is identified with the neutron. Further combinations of (u, d, s) quarks produce single strange or double strange baryons. Intriguing is the quark combination (uds), which can be used to generate either the Σ^0 [4] or the Λ hyperon. As indicated by the quark content both hyperons neither carry electro-magnetic charge nor I_3. However, the total isospin of Σ^0 amounts to 1, in contrast to Λ which

[2] Baryons containing at least one strange quark

[3] pp, p-Pb, Pb-Pb

[4] Note that unless explicitly specified all particles such as Σ^0 should be read like $(\Sigma^0 \oplus \overline{\Sigma^0})$

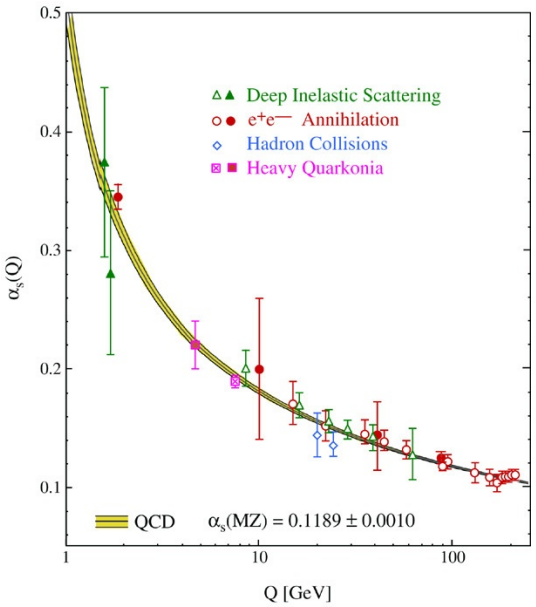

Figure 1.1: *The QCD coupling constant α_s with experimental data [1].*

has a total isospin of 0. Hence, the two hyperons have different isospin degeneracy factors g_i^{-1} associated with their respective ground states $g_{\Sigma^0} = 3$, $g_\Lambda = 1$. Their ratio dictates the expected value for the ratio of the two hyperon species,

$$\frac{\Sigma^0}{\Lambda} = \frac{g_{\Sigma^0}^{-1}}{g_\Lambda^{-1}} = \frac{g_\Lambda}{g_{\Sigma^0}} = \frac{1}{3} \ , \tag{1.2}$$

if the energy exceeds the threshold for the production of Σ^0. In Fig. 1.5 world data from different experiments on Σ^0/Λ as a function of $\sqrt{s}$ is summarized. Most of the recorded data is, within the uncertainties, consistent with a value of 1/3 for the ratio, which motivates the conclusion that in the probed energy regime no difference in the productions mechanisms for the two hyperons can be observed.

1.2 Study of confined, dense and cold QCD matter

Currently, no experiment is capable to probe the QCD phase diagram for low T with high values for μ_B, which are radically different conditions then produced at the LHC. However, as neutron stars (NS) are very dense cold remnants of stars weighing a few solar masses $M_\odot$, they can be regarded as natural readily available laboratories for the exploration of this region of the QCD phase diagram. In recent years, the data available on the masses and radii of NS has grown considerably as the

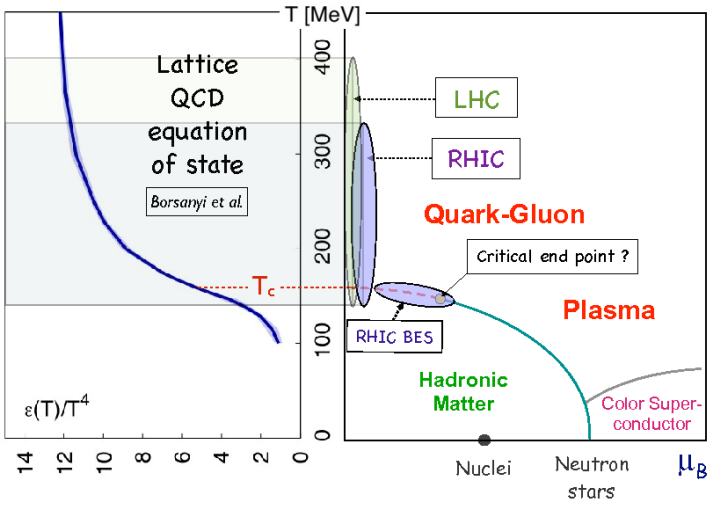

Figure 1.2: *QCD phase diagram with overlay of the experimentally covered regions by LHC and RHIC as well as the projection onto the predicted equation of state curve, obtained from Lattice QCD calculations, at $\mu_B = 0$ plotted via the temperature vs. energy density [2].*

instruments and theories have grown more sophisticated. The results obtained from these measurements are to this day not fully understood in terms of the implication for the NS composition and therefore for the equation of state (EOS) which governs the macroscopic features of the NS. For NS large values for μ_B are easily attained solely by the fact that these are very dense fermionic systems. In principle, μ_B can become sufficiently large that neutrons on the Fermi surface possessing the largest energy possible decay via weak interaction into hyperons. The newly produced hyperon then occupies a state in the Fermi sea of its own species. Each hyperon species produced is introducing a new degree of freedom to the system. The energy associated with each state depends on the interaction between the particle considered and the NS environment. The EOS for different assumptions about the composition of the NS are shown in Fig. 1.6. By including the Λ hyperon the EOS softens, but stiffens if phenomenological many-body interactions between Λ and nucleons are considered. However, with respect to the pure neutron matter hypothesis EOS, the EOS with incorporated Λ is always softer. This behaviour gives rise to the "hyperon puzzle", as of now no well-constrained EOS incorporating hyperons can produce NS with masses of up to $2M_\odot$, which is the most important experimental constraint for these kind of studies. This is seen by transforming the EOS in a relation between the mass and radius of the NS, with the help of the Tolman-Oppenheimer-Volkof equations, which describes hydrodynamically equilibrated matter while incorporat-

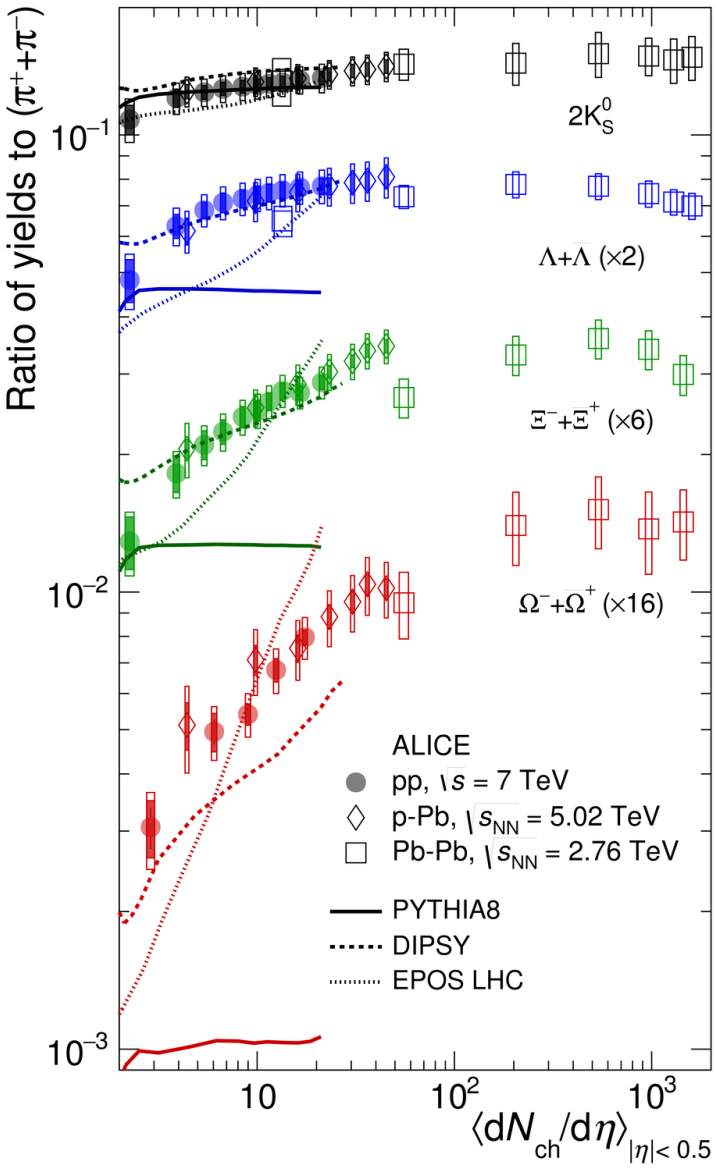

Figure 1.3: *Ratio of the p_{T}-integrated yield of hyperons to pions $(\pi^+ + \pi^-)$ as a function of the multiplicity of charged particles $\langle \mathrm{d}N_{ch}/\mathrm{d}\eta \rangle$ measured in $|y| < 0.5$. [4].*

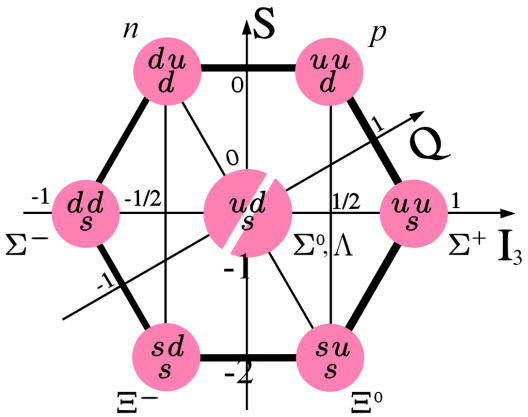

Figure 1.4: *Baryon octet showing the strangeness S, electromagnetic charge Q, third component of the isospin I_3 and quark content of all spin-1/2 baryons [5].*

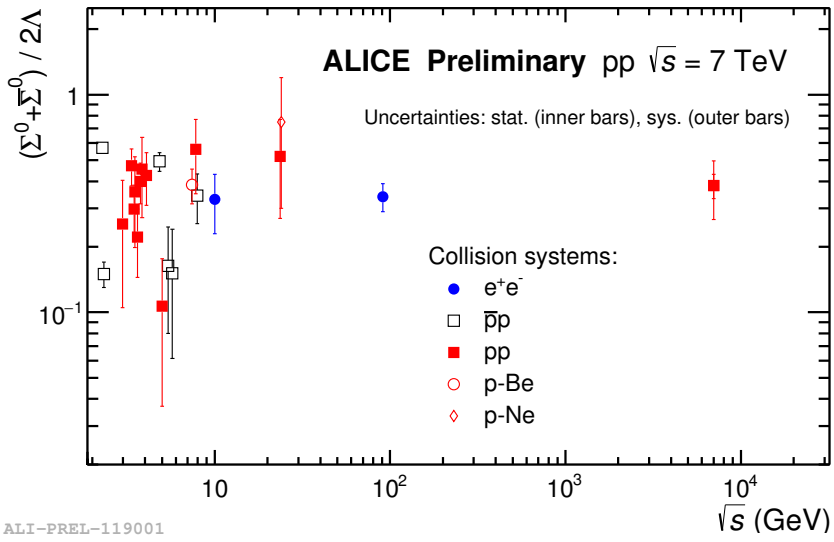

Figure 1.5: *World data of the Σ^0/Λ ratio [6].*

ing effects of general relativity. The results using the different EOS are shown in Fig. 1.6. Currently, the interaction between Λ and nucleons at nuclear density is experientially weakly constrained und unknown at larger densities. For other hyperons even fewer constrains on the interaction with nucleons is available. In the case of hyperons the most common approach to study particle interactions utilizes the study of hypernucleii or scattering experiments. These are in principle possible however difficult to realize due to the difficulties in generating a beam or (quasi-)target of hyperons such as Σ^0s or Ξs. A rather new method is to apply femtoscopy, which makes use of the two-particle correlation function,

$$C(k) = \int S(\boldsymbol{r}, k) \cdot |\Psi(\boldsymbol{r}, k)|^2 \mathrm{d}\boldsymbol{r} \xrightarrow{k\to\infty} 1 \ , \tag{1.3}$$

which is depending on the magnitude of the relative momentum vector $k = \frac{1}{2}|\boldsymbol{p_1} - \boldsymbol{p_2}|$ of the two ideally collinear moving particles and sensitive to the source term $S(\boldsymbol{r}, k)$ and most importantly to the 2-particle wave function $\Psi(\boldsymbol{r}, k)$, which incorporates the interaction between both particles. The determination of $C(k)$ from data is achieved by using the following relation,

$$C_k = \mathcal{N} \frac{N_{k,\mathrm{SameEvent}}}{N_{k,\mathrm{MixedEvent}}} \xrightarrow{k\to\infty} 1 \ , \tag{1.4}$$

where $N_{k,\mathrm{SameEvent}}$ refers to all combinations of particles which have been created in the same event, while $N_{k,\mathrm{MixedEvent}}$ references to combinations which show no correlation at all because particles produced in different events are combined. The normalisation factor is denoted by $\mathcal{N}$. Typically, femtoscopy is used to study the source, constraining its properties with pairs of particles of well-known interaction. However, by inverting the paradigm and making use of the previously fixed source the interaction between particle pairs, where the interaction is unknown, can be inferred. Starting from a potential V the solution of the Schrödinger equation delivers $\Psi(\boldsymbol{r}, k)$ and by employing a model for the source term $S(\boldsymbol{r}, k)$ the correlation function is obtained and then compared to the measured value.

One hyperon for which no detailed information on the interaction with nucleons is available is Σ^0. This is in part due to the circumstance that the state of the art technique to investigate Σ^0N interactions femtoscopy relies heavily upon the amount of gathered data. In the case of Σ^0 data gathered from ALICE is scarce because the reconstruction itself relies on the detection of a low energetic photon via conversion. However, more in depth knowledge about the nature of the hyperon-nucleon interactions would greatly help in constraining the different EOS models further and eventually resolve the "hyperon puzzle" leading to a better understanding of NS. On the other hand fixing the ratio Σ^0/Λ provides new insights in the corresponding production mechanism and final state interactions [8].

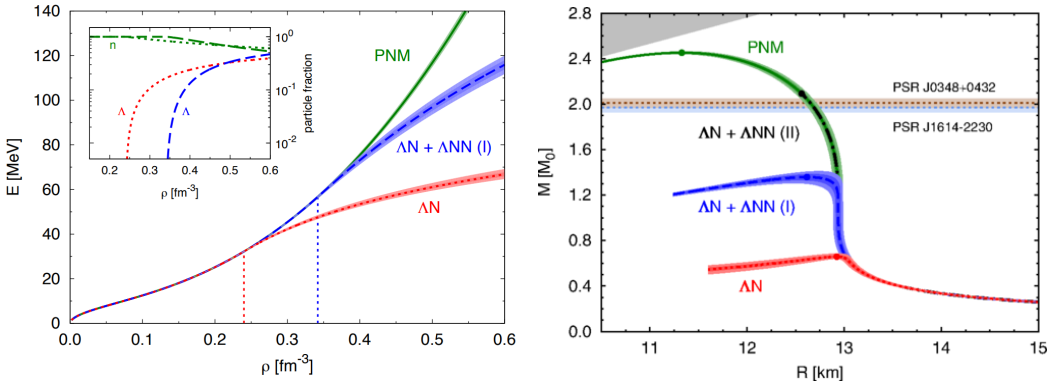

(a) (b)

Figure 1.6: *Equation of state (a) for different assumptions about the composition of the NS and interactions of the Λ with the NS matter. Relationship between the mass and the radius (b) of the neutron stars resulting from different approaches to the EOS. The green line shows the result for pure neutron matter, the red (blue) line includes the two (three) body ΛN(N). The uncertainties are represented by the coloured bands. The two horizontal bands indicate the masses of the heavy pulsars PSR J1614 − 2230 and PSR J0348 + 0432. The grey shadowed area is excluded because causality breaks down in this parameter space [7].*

Chapter 2

Analysis method

2.1 ALICE detector

The ALICE (A Large Ion Collider Experiment) detector [9], located at the LHC, is an experiment dedicated to studies of HI collisions and consists of 17 different sub-modules, which serve the purpose of enabling precise PID and track reconstruction. In Fig. 2.1, the schematic structure of ALICE, with the position of the different components is presented. The central cylindrical part of ALICE is permeated by a magnetic field of $B = 0.5$ T [9], which is generated by the L3 solenoid magnet (10 in Fig. 2.1). The field lines are collinear to the beam pipe. In the following, only the sub-modules which were used in the analysis for charged particle tracking, pile-up

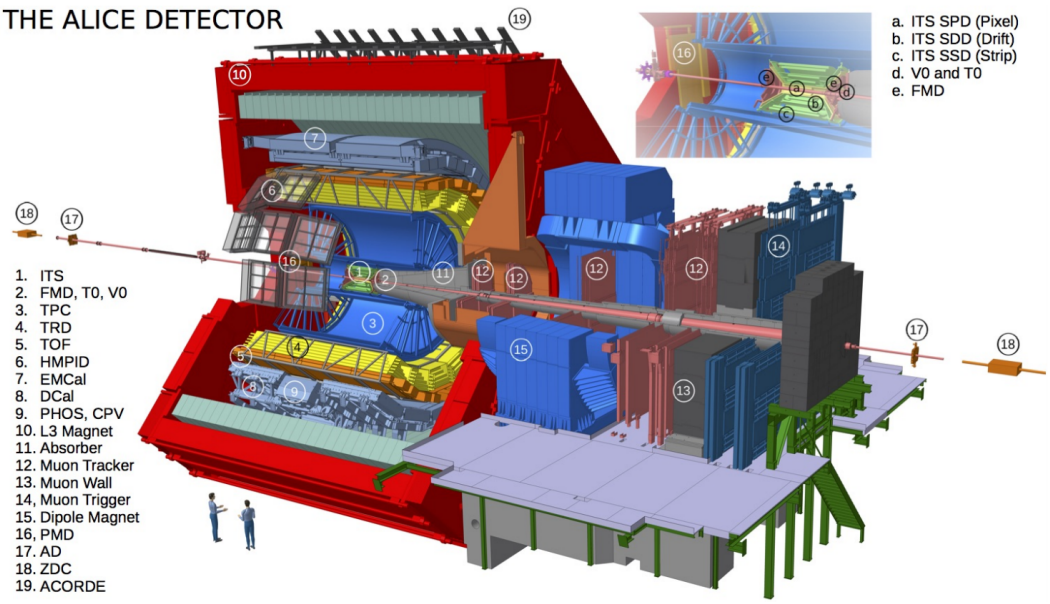

Figure 2.1: *ALICE detector with pointers to the submodules [9].*

removal and PID are briefly discussed.

The ITS (Inner Tracking System, 1 in Fig. 2.1) [9] is the innermost detector module and consists of 6 layers occupied by different silicon detectors (two innermost layers Silicon Pixel Detector (SPD), two intermediate layers Silicon Drift Detector (SDD) and two outermost layers Silicon Strip Detector (SSD)). It contributes to the full track reconstruction as well as pile-up removal with a momentum resolution of $\sigma_{\mathrm{p_T}}/\mathrm{p_T} \approx 10 - 12$ % [9]. It covers the whole $0 < \phi < 2\pi$ range of the azimuthal angle and pseudo-rapidities of up to $|\eta| < 0.9$ corresponding (by $\eta = -\ln(\tan\Theta/2)$) to polar angles in the range of $0° < \Theta < 135°$ [10]. In order to reduce multiple scattering of the produced particles the ITS was build from the lightest materials available e.g. carbon-fibres thus minimizing the material budget. The spatial resolution is on the order of magnitude of 10 µm [10] which suffices to deal with high multiplicities in HI collisions appropriately. The ITS is used for the reconstruction of primary and secondary vertices as well as enables PID.

The total sensitive volume of the TPC (Time Projection Chamber, 3 in Fig. 2.1) [10] is 90 m^3 with an inner (outer) radius of about 85 (250) cm, extending 500 cm in direction of the beam line. The TPC is needed for the reconstruction of 3-D tracks of charged particles. Due to the applied high voltage between central electrode and end-plates, the ionization electrons, liberated by the incident particles from the collision, are drifting to the end-plates for measurement. The drift time of these electrons in the TPC is maximally 100 µm [10]. During this time several LHC bunch crossings, and thus inelastic collision can occur. This leads to so-called out-of-bunch pile-up because not only the particles produced in the event which was triggered on will be recorded, but also particles from events which occured a full TPC drift time before and after the triggering. The reconstruction capability of the TPC is in parts due to the 159 radial rows which the particle, depending on its momentum and angle can traverse before leaving the TPC. This configuration allows to obtain the momentum of the particles with a resolution of $\sigma_{\mathrm{p_T}}/\mathrm{p_T} \approx 5$ % [9]. The coverage of the azimuthal angle as well as the pseudo-rapidities are equivalent to the ranges covered by the ITS [10]. The readout of the TPC is optimized to cope with the highest multiplicities in HI collisions and conducted with multi-wire proportional chambers which are located on the end-plates of the TPC.

In general PID is targeting to acquire information on the mass of the unknown particle. As in nature only certain masses are realized, it is a suitable physical property to differentiate between different particle species. Hence, indirect methods are employed by exploiting the energy momentum relation[1], which links the particles

[1] For simplicity c is set to equal 1

momentum p with the non-zero rest-mass m_0,

$$\beta = v = \frac{\gamma m_0 v}{\gamma m_0} = \frac{p}{E} = \frac{p}{\sqrt{m_0^2 + p^2}} \qquad \Rightarrow \qquad m_0 = p\frac{\sqrt{1-\beta^2}}{\beta} = \frac{p}{\beta\gamma} \ . \tag{2.1}$$

An expression for m_0 depending on the fraction of the particles velocity v with respect to the speed of light c denoted by $\beta = v/c$ and p is obtained. Therefore, PID in essence strives to realize measurements of β and p in order to determine m_0. PID for the particles traversing the gas filled sensitive volume of the TPC is conducted by measuring the energy loss occurring due to ionization $\mathrm{d}E/\mathrm{d}x$, is described by the Bethe-Bloch (BB) formula,

$$-\left\langle \frac{\mathrm{d}E}{\mathrm{d}x} \right\rangle = \frac{4\pi n z^2}{m_e c^2 \beta^2} \cdot \left(\frac{e^2}{4\pi\epsilon_0} \right)^2 \cdot \left[\ln\left(\frac{2 m_e c^2 \beta^2}{I \cdot (1-\beta^2)} \right) - \beta^2 \right] \ . \tag{2.2}$$

The mean energy loss over a distance $\langle \mathrm{d}E/\mathrm{d}x \rangle$ for a particle with charge z moving with the velocity v in a material with electron density n depends on the mass of electrons m_e and the vacuum permittivity ϵ_0. As $\langle \mathrm{d}E/\mathrm{d}x \rangle$ is a function of β and hence can also be parametrised with $\beta\gamma$ by additionally making use of Eq. 2.1, the dependency is equal to p/m_0. Therefore this method is applicable for PID because the mass dependency introduces distinguishable mass bands as long as p is not much larger than m_0, as shown in Fig. 2.2. These can then be selected by applying the $n_\sigma-$identification method. First, an ideal BB curve is obtained by solving Eq. 2.2 under a certain particle hypothesis, which fixes m_0. The measurement is then compared to this hypothesis and the discrepancy expressed in multiples of the detector resolution σ. The smaller n is chosen the more likely it is for the reconstructed particle to correspond to the hypothesis used to obtain the ideal BB curve.

The TOF (Time Of Flight, 5 in Fig. 2.1) [12] consists of 1593 glas Multi-gap Resistive Plate Chamber detectors, which in total provide 148149 read-out pads. The coverage of the azimuthal angle as well as the pseudo-rapidities is equivalent to the ranges covered by the ITS. Measurements of the ITS and TPC are complemented by the TOF, which measures the time of flight of the particle allowing to determine β. The time resolution of the TOF is around 80 ps [12] which is vital in order to conduct precise PID and enables to remove out-of-bunch pile-up. Because of the magnetic field, only particles which reach a certain transverse momentum p_T are able to reach the TOF. PID is conducted on the same principle as discussed above, by relying again on Eq. 2.1 and making use of the $n_\sigma-$identification method.

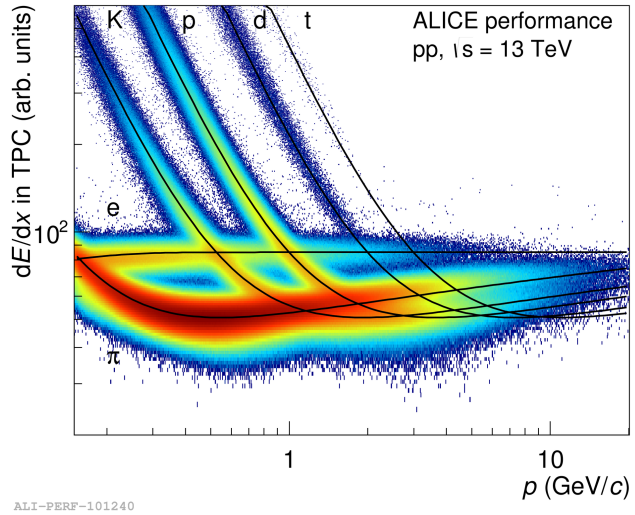

Figure 2.2: *Measurement of* $\mathrm{d}E/\mathrm{d}x$ *with ideal Bethe-Bloch curves [11].*

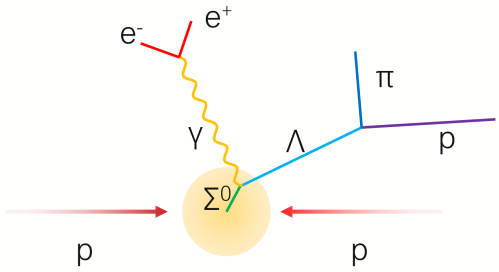

Figure 2.3: *Illustration of the* Σ^0 *into* $\Lambda\gamma$ *and the subsequent decay of the* Λ *in* $p\pi^-$ *and the pair creation of the photon.*

2.2 Event topology

An illustration of the Σ^0 decay mode, targeted in this analysis, is presented in Fig. 2.3. The branching ratio for the $\Sigma^0 \rightarrow \Lambda\gamma$ decay mode is approximately 100 % [13] and about 63.9 % [14] for the subsequent decay $\Lambda \rightarrow \mathrm{p}\pi^-$. The boost received by the photon from the decay is quite low because most of the momentum is carried away by the massive Λ. The lower bound for the energy carried by the photon is equal to the difference in mass between Σ^0 and Λ of about 76 MeV [13]. Thus, neither the detection via the electromagnetic calorimeter EMCAL (Electromagnetic Calorimeter, 7 in Fig. 2.1), which has a threshold of $\approx$ 140 MeV surpassing the energy of the photon nor via PHOS (Photon Spectrometer, 9 in Fig. 2.1), which shows a large combinatorial background, as seen in Fig. 2.4, is satisfactory. Addi-

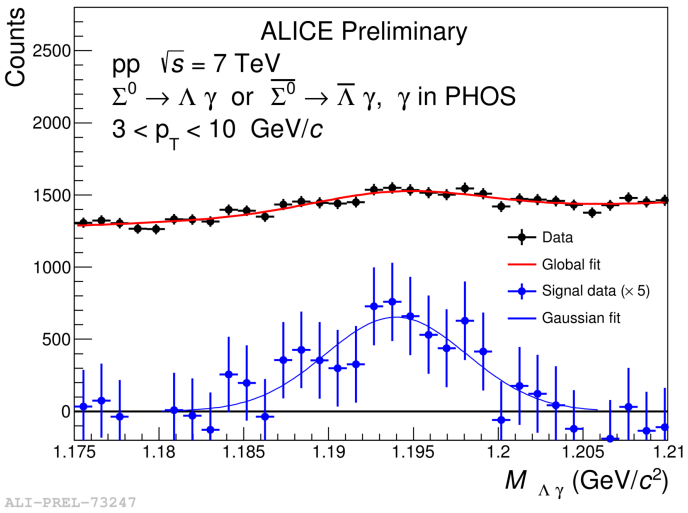

Figure 2.4: *Measurement of* Σ^0*, where the photon was detected with the ALICE PHOS calorimeter [15].*

tionally, the limited geometrical acceptance of EMCAL and PHOS are detrimental to the detection. Instead, the indirect detection of the low energy photon shows a higher resolution and is thus favourable. This is achieved by reconstructing the photon from e^+e^- originating from pair-creation. The probability of photon conversion increases with the energy of the photon as seen in Fig. 2.5 and dominates above energies of 5 MeV. With an minimum energy of about 76 MeV, carried by the photon, conversion in matter is the preferred channel. This method, however, requires precise knowledge of the material budget of the detector. In Fig. 2.6 reconstructed photon conversion vertices within the ALICE detector are shown, as expected the regions with the most dense material show the highest rate of photon conversions. Considering only the central barrel of ALICE the conversion probability amounts to about 8 % [16]. The kinematics of the e^+e^- pair make a detection of the photon impossible if the p_T of the daughter tracks is smaller than about 100 MeV/c as in this case the trajectories are curling in the magnetic field, which are then exempted from reconstruction. Moreover, the PID capabilities are limited as for low p the mass bands of electrons and pions overlap. Although these conditions make the analysis a challenging task with the help of Monte Carlo (MC) simulations it is possible to significantly improve the PID capabilities. This is achieved in two steps, first the characteristic properties of the e^+e^- pairs are determined, in the following, with this knowledge the selection criteria for the analysis are carefully optimized.

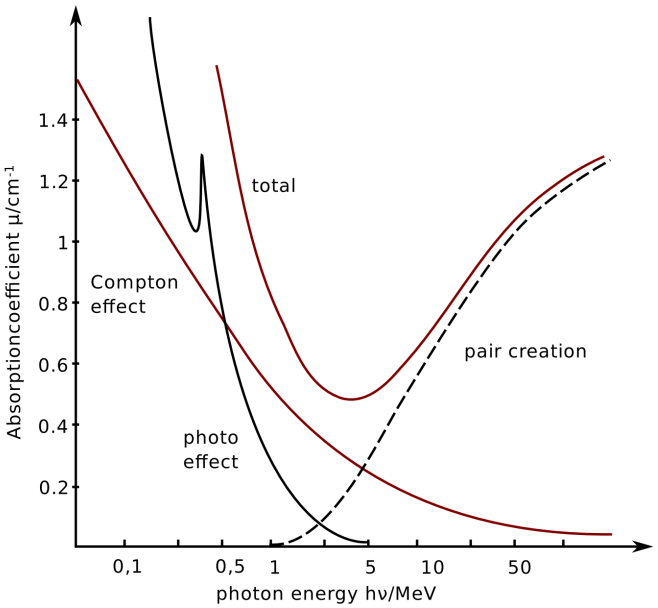

Figure 2.5: *Contribution to the absorption-coefficient of various interactions between the photon and matter depending on the energy of the photon [16].*

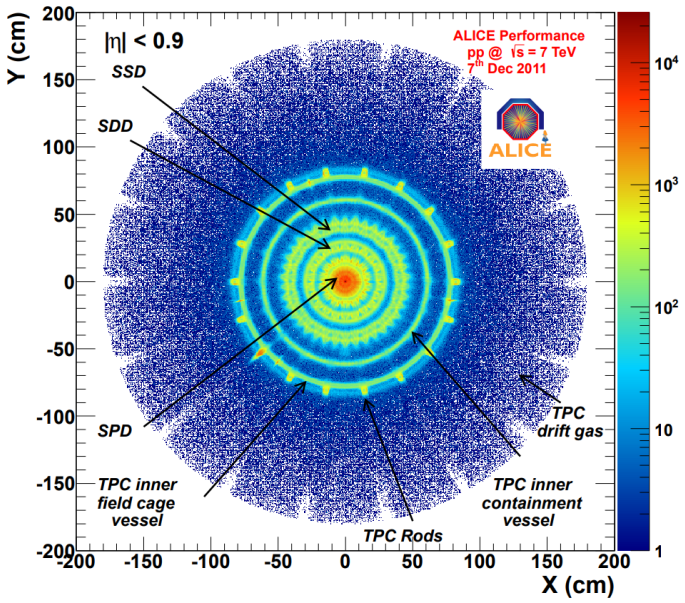

Figure 2.6: *Distribution of the reconstructed photon conversion points in X vs. Y in the fiducial area. The different subsystems are indicated by vectors. [16].*

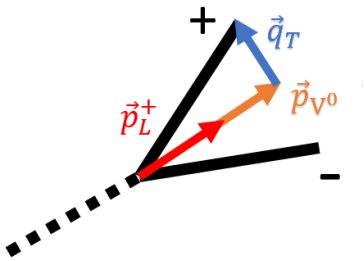

Figure 2.7: *Schematic depiction of a* V^0 *topology where the two oppositely charged daughter particles share the same mass. The orange (red/blue) vector represent the total (longitudinal/transverse) momentum of the (positively charged daughter particle with respect to the total momentum of the)* V^0.

2.3 Structure of the Analysis

As discussed in the previous section the challenge in reconstructing Σ^0 is the reconstruction of the photon. In order to reconstruct the photon the dedicated task[2] for photon conversions of the PCM[3]-Group was used. For the analysis, pass 1 data in the ESD format, gathered from 2016 and 2017 in pp collisions is used. This amounts to 1.04×10^9 minimum bias events.

2.3.1 Reconstruction of the photon

As neither the hyperons nor the photon carry an electromagnetic charge they will not ionize the drift gas of the TPC and are not seen by the detector. Therefore, only the reconstructed trajectories of the charged decay products of $\Lambda \rightarrow p\pi^-$ and the e^+e^- pair from photon conversion will be visible. Each will leave a characteristic shape in the form of a "V" (and because they originate from a neutral charged particle these secondary vertices are named V^0) in the detector, as schematically depicted in Fig. 2.7. Considering the sizeable overlap of the pion and electron dE/dx bands in low p ranges additional methods to do PID have to be employed. In the following each method used for the photon PID will be introduced.

The Armenteros-Podolanski-cut constrains two parameters, which are measured with respect to the mother particle momentum P_{V^0}. The first one is the degree of symmetry of the longitudinal momenta p_L of the two daughter particles denoted by

[2] Available at AliPhysics/PWGGA/GammaConv at the time of the analysis
[3] photon conversion method

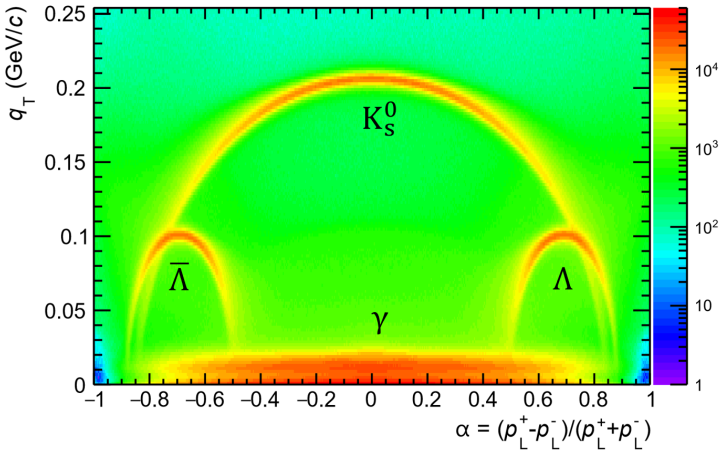

Figure 2.8: *Armenteros-Podolanski-Plot. The mass bands for the different particles are labelled according to their species.*

$$\alpha = \frac{p_L^+ - p_L^-}{p_L^+ + p_L^-} \ , \tag{2.3}$$

where the plus and minus sign indicate to which of the oppositely charged daughters p_L belongs. The second is the transverse momentum q_T, also measured with respect to P_{V^0}, of the two daughter particles, which is equal for both daughters because of the conservation law for the momentum. As the photon does not carry any rest-mass, the trajectories of e^+ and e^- should be collinear at the point of conversion, which results in very low values for q_T. Making use of the specific decay topology, the cut imposed on the Armenteros-Podolanski-parameters is one of the most important selection criterion employed for PID in the analysis. Because the p_L received by the daughters depends on their masses for equal masses one expects a distribution of α symmetric around 0, whereas for unequal masses of the daughters the distribution is shifted, as shown in Fig. 2.8. The ellipses correspond to different particles, the upper central one is caused by K^0_s, the symmetrical distributed ellipses on the sides appear because of $\Lambda \to p\pi^-$ (right) and the corresponding decay of $\overline{\Lambda}$ (left). The intensity at the bottom is stemming from $\gamma \to e^+e^-$. The bands for K^0_s and the photon are distinguishable because K^0_s has, in contrast to the photon a non-vanishing rest-mass which boosts the daughters. The regions where the bands are separated enable precise PID, especially if used in conjunction with other identification criteria.

As discussed above the trajectories of e^+ and e^- are collinear. Consequently the angle between the e^+e^- pair is purely due to the Lorentz force of the magnetic

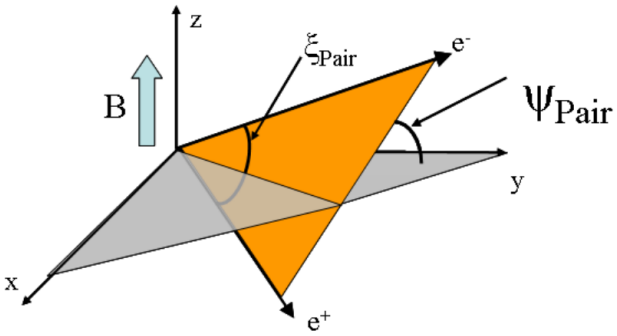

Figure 2.9: *Depiction of the orientation of the* e^+e^- *pair with the magnetic field B in z direction. The angle* ξ_{Pair}*, between the* e^+e^- *pair, lies within the orange plane spanned by the momenta of the pair. The x-y plane is perpendicular to the direction of B [17].*

field forcing a bending in azimuthal direction. This gives rise to another method of distinguishing pairs of e^+e^- originating from the conversion of the photon from uncorrelated e^+e^- pairs. Only e^+e^- pairs stemming form photon conversions will exhibit small values for the angle,

$$|\Psi_{\text{Pair}}| = \arcsin\left(\frac{\Delta\vartheta}{\xi_{\text{Pair}}}\right) \tag{2.4}$$

between the plane spanned by the e^+e^- pair and the plane perpendicular to the magnetic field, as shown in Fig. 2.9. The difference between the angle of the momentum of e^+ and of e^- with the direction of the magnetic field B is denoted by $\Delta\vartheta$. The angle between e^+ and e^- is described by ξ_{Pair}.

The pointing angle α is defined as the angle between the vector, connecting the primary to the conversion vertex in Fig. 2.10, and $\boldsymbol{P}_{\text{V}^0}$. By demanding small α it is ensured that the photon is not a by-product of interactions between the collision products and the material of the detector.

In order to ensure only tracks with of good quality were used for the analysis, track selection criteria were applied. By restricting the η selection it is secured that particles, which traversed the detector were measured with the best resolution available. The more data on the track is available the easier is the reconstruction. Demanding a certain ratio of findable TPC clusters were used for the track reconstruction leads to a higher accuracy of the tracks parameters. The findable ratio of TPC clusters is calculated by dividing the number of detected TPC clusters by the number of rows the particle could have traversed and left a signal in. And

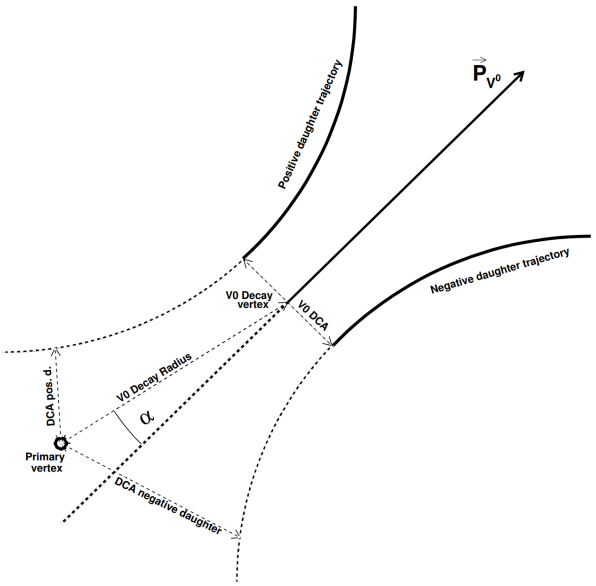

Figure 2.10: *Schematic structure of secondary vertices. The vector* $\boldsymbol{P}_{\mathrm{V0}}$ *refers to the momentum of the mother particle. The acronym "DCA" stands for distance of closet approach [18].*

finally in order to assign the daughter tracks correctly to a secondary vertex, the distance of closest approach (DCA) of the daughter tracks to the secondary vertex is constrained.

No out-of-bunch pile-up removal is done by using the information available on the photon. The assignment of Σ^0 to an event is done by making use of the detected Λ. A summary of the applied cuts and their correspondingly tuned values used for the reconstruction of the photons is presented in Tab. 2.1. The resulting invariant mass spectrum for the photons is shown in Fig. 2.11. The by far biggest contribution in this figure stems from photons with a very small invariant mass as expected.

2.3.2 Reconstruction of Λ and pile-up handling

As for the reconstruction of the photon one important method is the Armenteros-Podolanski-cut, which in this case is tuned to select Λ. Further, a mass selection criterion is imposed on the invariant mass of the decay products in order suppress the remaining combinatorial background. Out-of-bunch pile-up for Λ is removed by employing a track-based selection method. As discussed before the information gained by the ITS and TOF are used. By either requiring a hit in the SPD or SSD

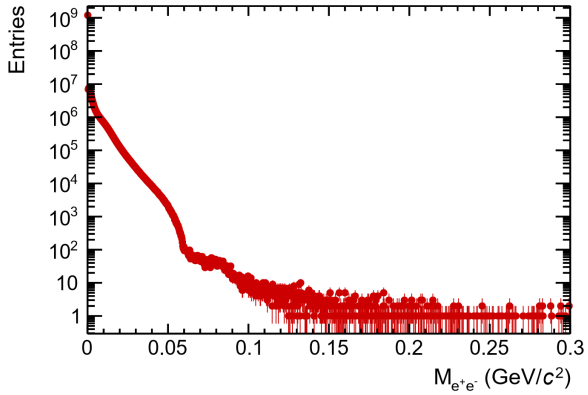

Figure 2.11: *The invariant mass spectrum of the photon, after the application of all cuts.*

Table 2.1: *Summary of selection criteria with values used for the reconstruction of the photon.*

Cuts for γ	
V^0-Finder-Type	online
η	0.9
Radius of conversion R	$5 - 180$ cm
Ratio of findable TPC clusters	35 %
n_σ- identification for e^+/e^-	-6 below and 7 above $\langle dE/dx \rangle_e$
n_σ- identification for π^+/π^-	-10 above $\langle dE/dx \rangle_\pi$
min. p_T for n_σ- identification for π^+/π^-	0.5 GeV/c
max. p_T for n_σ- identification for π^+/π^-	100 GeV/c
Maximum q_T cut	0.06 GeV/c
Max. χ^2 cut for γ	30
$\lvert\Psi_{Pair}\rvert$ on the angle between the e^+e^- pair	0.2 and triangle cut with χ^2
Range of α	$< \lvert 1 \rvert$
Minimun cos P.A. (α) of γ	0.99

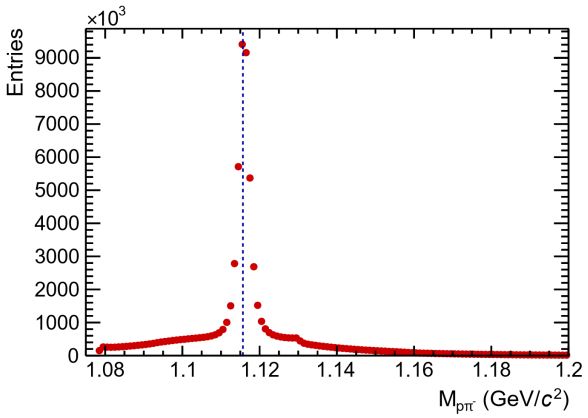

Figure 2.12: *The invariant mass spectrum of* Λ*, after the application of all cuts. The blue dashed line represents the DPG [14] value of the mass of* Λ*.*

layers[4] of the ITS or via the timing information gained by the TOF for one daughter. Similar track quality and topological selection criteria are employed as in the case of the photon, see Tab. 2.2. The invariant mass spectrum of the reconstructed Λ obtained form data, is shown in Fig. 2.12. The pronounced peak is well in agreement with the PDG value of (1115.683 ± 0.006) MeV [14] for the mass of Λ.

[4]SDDs are excluded due to the low timing resolution

Table 2.2: *Summary of cut parameters with values used for the reconstruction of* Λ.

Cuts for Λ	
V^0-Finder-Type	offline
η	0.8
Radius of conversion	$0.2 - 100$ cm
p_T cut on Λ	0.3 GeV/c
Ratio of findable TPC clusters	70 %
n_σ- identification for p	5
Minimum q_T cut	0.30 GeV/c
Maximum q_T cut	0.95 GeV/c
Max. χ^2 cut for Λ	4
Range of α	$0.01 - 0.12$ (negative for $\overline{\Lambda}$)
Minimum $\cos(\alpha)$ of Λ	0.99
n_σ- identification for Λ	5 around $\langle \mathrm{d}E/\mathrm{d}x \rangle_\Lambda$
Mass for Λ selection	$0.008 < m_{\Lambda,\mathrm{PDG}} < 0.008$
DCA of the daughters to the primary Vertex	$0.05 - 1.50$ m
Pile-Up rejection mode	Daughter hits in either ITS or TOF

Chapter 3

Results and discussion

3.1 Monte-Carlo studies

In order to identify characteristic features, enabling the separation of signal γ_{Σ^0}, originating from the decay of Σ^0, from background, Monte-Carlo (MC) simulations were employed. The usefulness of these simulations lies within in the fact, that all identities of all produced particles are known without any ambiguity. By applying the analysis to a MC generated data sample, the true particle type can be accessed afterwards by using the information from the simulation. This enables a precise study of the particle properties and the kinematics, which depends on the production mechanism. The MC event generator used in this analysis is PYTHIA 8 [19], which is dedicated to simulate particle collisions and widely used in high energy physics [20]. The distribution of $|\Psi_{Pair}|$ as a function of p_{T} for γ^{Truth}, which are verified to be proper photons by making use of MC information, is shown in Fig. 3.1 and for identified background in Fig. 3.2. In the region with low p_{T} and values close to 0 for $|\Psi_{Pair}|$ most of the γ^{Truth} are located. The $|\Psi_{Pair}|$ for the background is distributed rather smoothly and predominantly found in regions with low p_{T}. Therefore cutting on low values for $|\Psi_{Pair}|$ results in a high ratio of signal to background. By making use of the MC information it is possible to distinguish and hence to compare the characteristics of γ^{Truth} and of $\gamma_{\Sigma^0}^{Truth}$. The index "$\Sigma^0$" denotes that it was secured via MC information, that the photon is a product of the decay of Σ^0. One of the findings is presented in Fig. 3.3, where the p_{T} distributions of both types of photons are shown. As significantly more γ^{Truth} than $\gamma_{\Sigma^0}^{Truth}$ are produced the distribution of γ^{Truth} was rescaled by a factor of 1.2×10^{-3} in order to make the distributions comparable. The difference in the width and peak position of the two distributions are clearly visible.

3.2 Σ^0 yield

The invariant mass $\mathrm{M}_{\Lambda\gamma}$ spectrum, which also includes pairs of $\overline{\Lambda}\gamma$, obtained from the data is shown in Fig. 3.4. The total $p_{\mathrm{T}}-$integrated yield of Σ^0 obtained by the cuts discussed above amounts to (24162 ± 315) particles, which is an increase

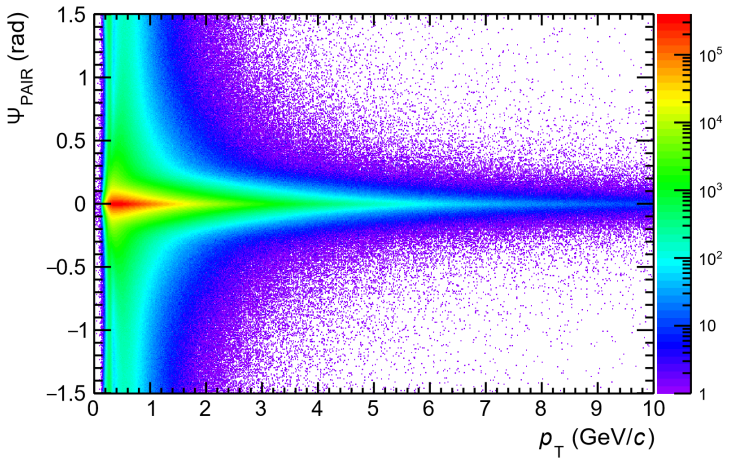

Figure 3.1: $|\Psi_{Pair}|$ *vs.* p_{T} *for* γ^{Truth} *only.*

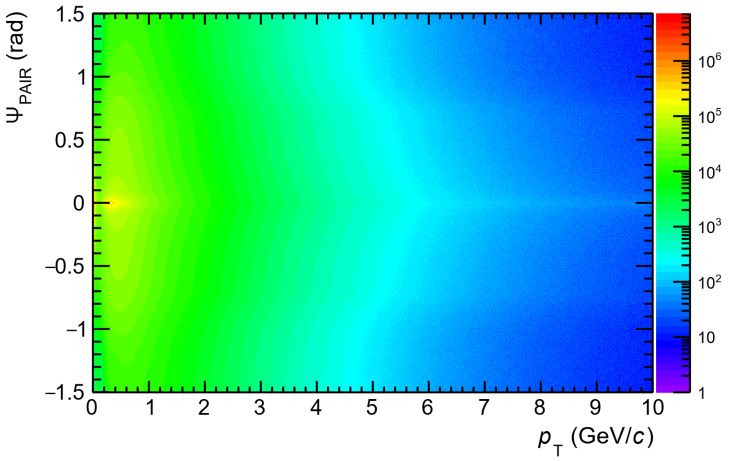

Figure 3.2: $|\Psi_{Pair}|$ *vs.* p_{T} *for background only.*

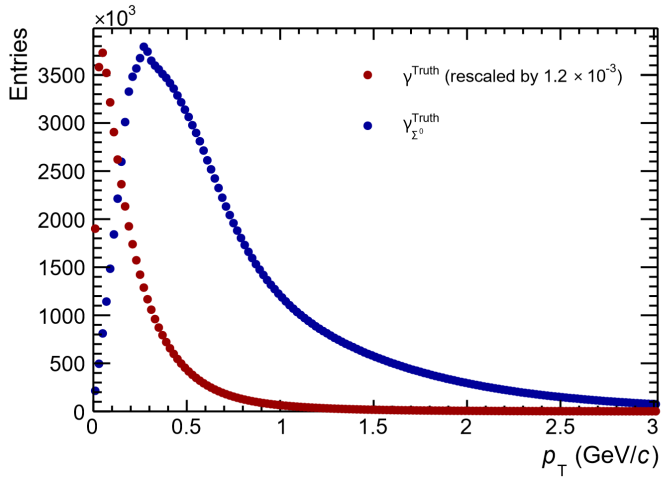

Figure 3.3: *The p_{T} distributions for γ^{Truth}s and $\gamma^{Truth}_{\Sigma^0}$. A rescaling of 1.2×10^{-3} was applied to the γ^{Truth} data.*

of a factor of about 2.5, if compared to the yield gained with the non-optimized cut parameters. For the extraction of the signal the background was fitted with a polynomial of 4th order and then subtracted from the $\mathrm{M}_{\Lambda\gamma}$ spectrum. In order to fit the signal a single Gaussian distribution was found to be sufficient. Then, the yield was extracted by counting the bins in the range of $\pm$ 5 MeV/c with respect to the mean value M_{Σ} of the signal, which corresponds to about 3 times the width σ_{Σ} of the signal. The uncertainties associated with M_{Σ} respectively σ_{Σ}, for the $p_{\mathrm{T}}-$integrated spectrum, are on the order of a few percent. The $\mathrm{M}_{\Lambda\gamma}$ spectra in p_{T} bins at mid-rapidity $|y| < 0.5$, are shown in Fig. 3.5. For the signal extraction of the $p_{\mathrm{T}}-$binned spectra instead of the fit, the mixed event background (MEB) was subtracted from the signal, because it showed stable results for all p_{T} bins. The MEB is attained by calculating the invariant mass of the pairs $\Lambda^{\mathrm{mix}}\gamma$ and $\Lambda\gamma^{\mathrm{mix}}$. The particles with no index come from the initial event while the index 'mix' indicates the particles were taken from another event. For the mixing particles from 10 events were used. The gain in applying this method is to get an estimate of the shape of the combinatorial background in the signal region. As particles of different events can not be correlated they do not contribute to the signal of the correlated pairs. Because the MEB has much more entries than the data, a normalisation has to be applied. The normalisation is done by requiring that the integral of the MEB and the signal return the same value for a control region, which excludes the signal. For all $p_{\mathrm{T}}-$binned spectra the same control region of 1.2 GeV/c^2 $< \mathrm{M}_{\Lambda\gamma} <$ 1.235 GeV/c^2 was used. The signal histogram is then obtained by subtracting the MEB from

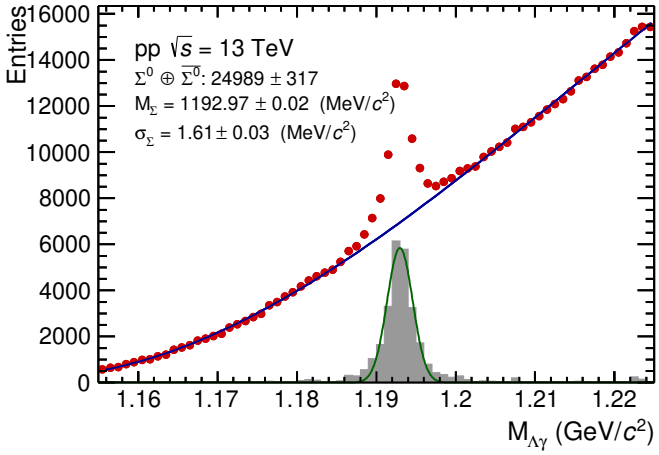

Figure 3.4: *Invariant mass* $M_{\Lambda\gamma}$ *distribution of* Σ^0 *depicted with red dots. The background (signal) is fitted with a polynomial of 4th order (single Gaussian distribution).*

the data and was fitted using again a single Gaussian distribution. The values for M_Σ, σ_Σ as well as for the raw yield of Σ^0 have been determined for each p_T bin individually. In Fig. 3.6, σ_Σ as a function of p_T is shown, for comparison the values of σ_Σ attained by the same method from MC data are also shown. Likewise in Fig. 3.7 the values for M_Σ are shown for data and MC. The consistency demonstrates that signal extraction and detector resolution effects are well under control. The extracted yield as a function of p_T is shown in Fig. 3.8. The raw yield of Σ^0 peaks at the p_T range of 2.20 GeV/c < p_T < 2.30 GeV/c. Although most of the yield is expected to be below the range of p_T < 1 GeV/c, these regions are very difficult to access experimentally, due to the acceptance effects and efficiency of the track reconstruction. In comparison to the PDG value of (1192.642 ± 0.024) MeV [13] for the mass of Σ^0 the obtained values for M_Σ deviate in the range of about 1.1 ‰. Only statistical uncertainties were accounted and propagated. Sources which would contribute to systematic uncertainties such as the material budget of the detector are neglected, due to the fact that a detailed analysis of the systematic uncertainties lies beyond the scope of this work.

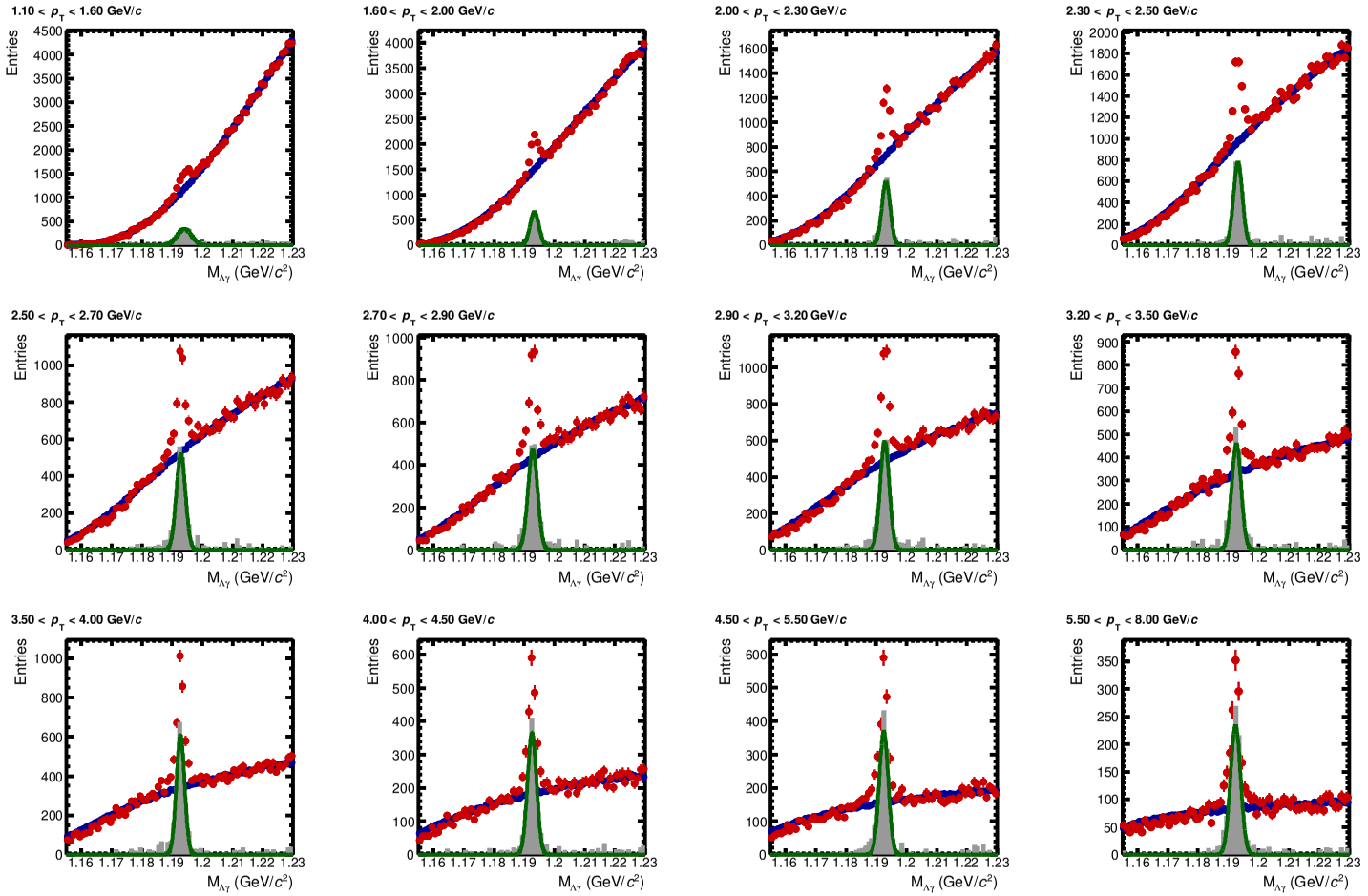

Figure 3.5: *Invariant mass* $M_{\Lambda\gamma}$ *distribution of* Σ^0 *(mixed event background) in* p_T *bins at mid-rapidity* $|y| < 0.5$ *depicted with red (blue) dots. The signal (green) was fitted with a single Gaussian distribution.*

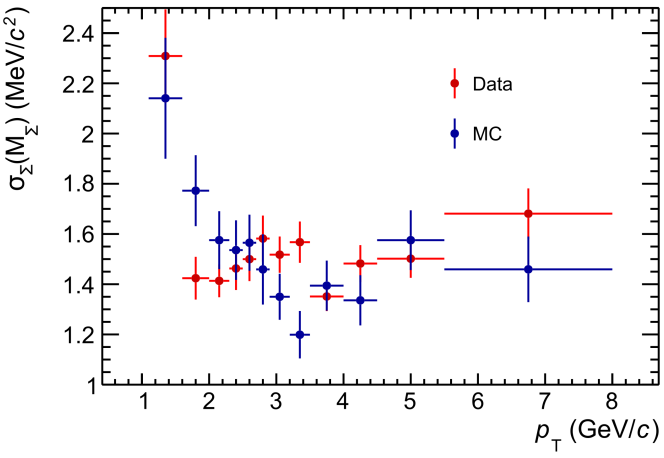

Figure 3.6: *Width σ_Σ of the Gaussian distributions fitted to the signal as a funktion of p_T.*

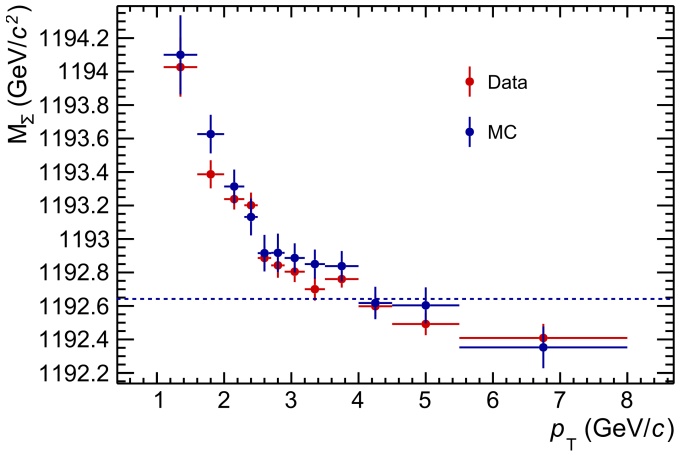

Figure 3.7: *Mean value M_Σ of the Gaussian distributions fitted to the signal in the different p_T bins. The PDG [13] value for the mass of Σ^0 is indicated with the dashed blue line.*

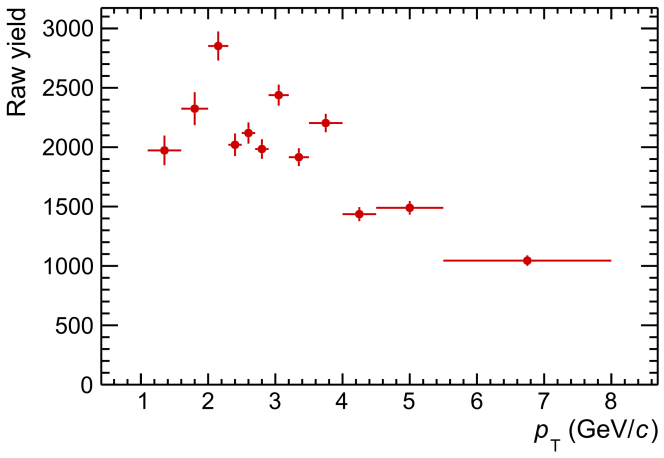

Figure 3.8: *Raw yield of* Σ^0 *as a function of* p_T.

3.3 Efficiency and purity

The efficiency $\varepsilon_{rec\times acc}$ is defined as:

$$\varepsilon_{rec\times acc} = \frac{Y^{rec\times acc}}{Y^{gen}} \ , \tag{3.1}$$

where the yield of all particles, which are recorded (generated) are denoted by $Y^{rec\times acc}$ (Y^{gen}). The quantity $\varepsilon_{rec\times acc}$ is thus a measure of acceptance effects of the detector systems. An ideal detector, capable of detecting every in the event produced particle, in combination with an ideal analysis capable of assigning every particle the right identity, yields the optimal value of 1. Thus the range anticipated for $\varepsilon_{rec\times acc}$ lies between 0 and 1. By employing Eq. 3.1, $\varepsilon_{rec\times acc}$ was obtained from the ratio of the reconstructed MC yield and the MC distribution of the generated Σ^0, shown in Fig. 3.9 and in Fig. 3.10. In Fig. 3.11 the values for $\varepsilon_{rec\times acc}$ are shown for Σ^0 in every p_T bin. The magnitude of the values for $\varepsilon_{rec\times acc}$ are expected due to the circumstance that for the photons only a probability of 8 % for conversion is given and multiplied with the efficiencies of the photon and Λ as well as branching ratios of the decay modes. The cause for the low values of $\varepsilon_{rec\times acc}$ for small p_T lies predominantly with the dropping detector acceptance, as mentioned before tracks which $p_T < 100$ MeV/c will curl in the magnetic field and are exempted from the reconstruction algorithm. The cuts used for the generated MC dataset are the exactly the same cuts as in the analysis.

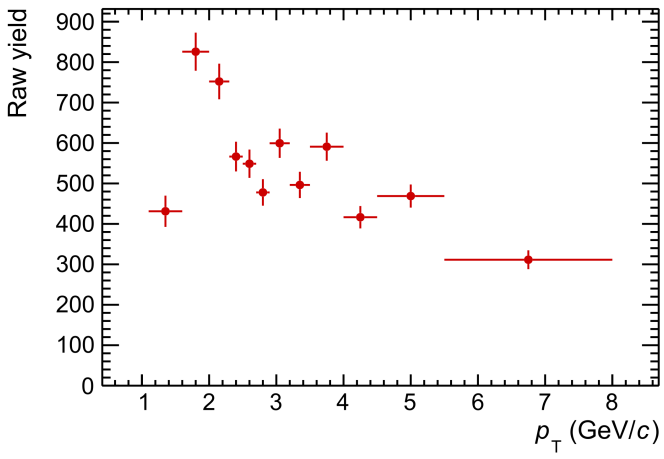

Figure 3.9: *Raw yield of the MC dataset of* Σ^0 *as a function of* p_T.

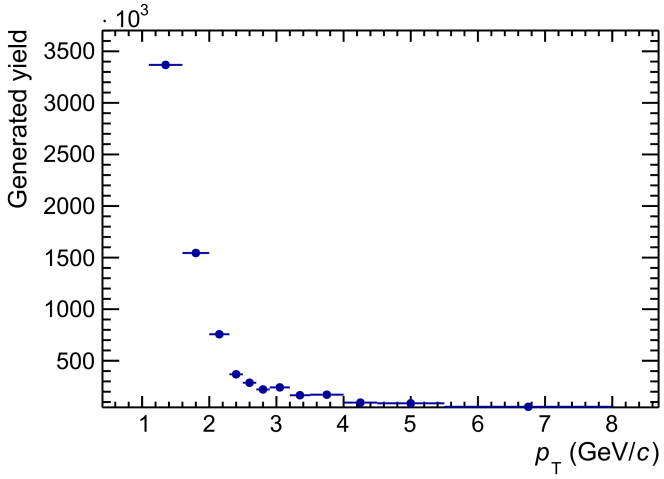

Figure 3.10: *Yield of the MC dataset of all generated* Σ^0 *as a function of* p_T.

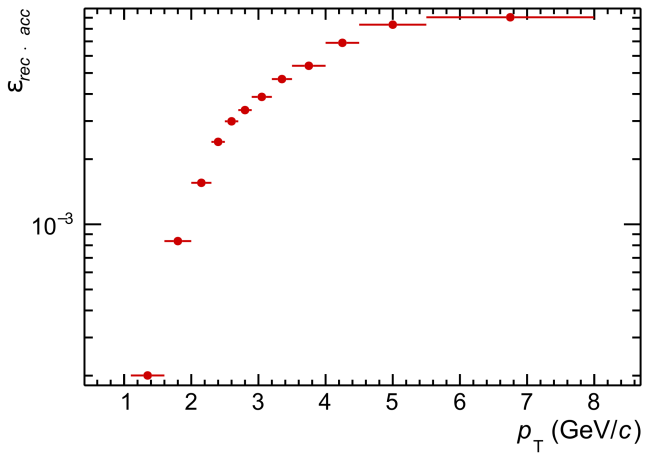

Figure 3.11: *Efficiency of reconstruction and acceptance as a function of* p_T.

A measure of the signal extraction for analyses is the purity calculated by:

$$\text{purity} = \frac{S}{S+B} \ , \tag{3.2}$$

where S (B) refers to the raw yields of the signal (background), extracted with the methods described in the previous section. As for the efficiency, the value of the purity lies between 0 and 1. The higher the value the better the signal can be discriminated from the background. For each p_T bin the purity was calculated, the results are shown in Fig. 3.12. The input for S are the extracted yields shown in Fig. 3.8, for B the mixed event background was integrated within the same range, of $\pm$ 5 MeV/c with respect to M_Σ, as the signal. The decrease of the purity with smaller p_T can also be attributed to the detector acceptance. The p_T averaged value was calculated to be 26.4 %.

3.4 Corrections applied the invariant mass spectra of Σ^0 in p_T bins

In order to describe reality more accurate the raw data, shown in Fig. 3.8, obtained from the experiment has to be corrected. The effects which have to be taken in account, as a correction factor on the yields, are attributed to properties of the detector as well as the imperfect particle identification by the analysis. Both effects are accounted for in the calculated $\varepsilon_{\text{rec}\times\text{acc}}$. By dividing each bin with the corresponding $\varepsilon_{\text{rec}\times\text{acc}}$ the p_T spectra are corrected and reflect what a perfect measurement would

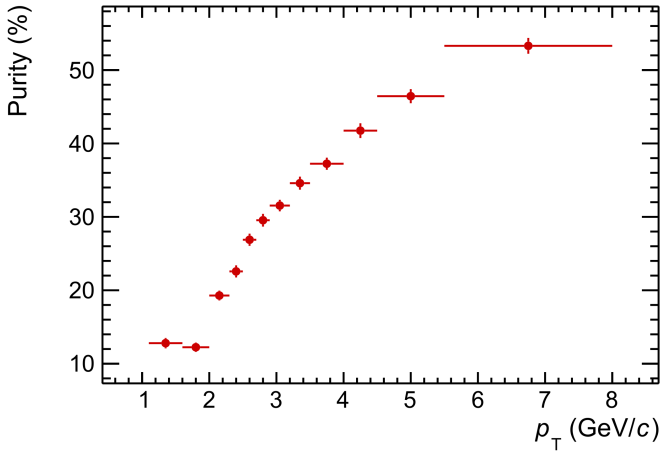

Figure 3.12: *Calculated purity as a function of* p_{T}.

look like. Furthermore, in order to compare the yields of Λ and Σ^0 as accurately as possible an extrapolation of the spectra for the low p_{T} range of 0 up to 1.1 GeV/c, where no data-points are available, has to be attained. The extrapolation is obtained by fitting a Levi-Tsallis function,

$$\frac{1}{N_{\mathrm{inel}}}\frac{\mathrm{d}^2N}{\mathrm{d}y\mathrm{d}p_{\mathrm{T}}} = \frac{(n-1)(n-2)}{nC[nC+m_0(n-2)]}\frac{\mathrm{d}N}{\mathrm{d}y}p_{\mathrm{T}}\left(1+\frac{m_{\mathrm{T}}-m_0}{nC}\right)^n \tag{3.3}$$

to $p_{\mathrm{T}}-$binned spectrum, normalized to the inelastic pp collisions. The total occurrences of inelastic pp scatterings are denoted by N_{inel}. The transverse mass is defined by $m_{\mathrm{T}} = \sqrt{m_0^2+p_{\mathrm{T}}^2}$. And $\mathrm{d}N$, n and C are three free parameters, which are determined by the fit. Because the Levi-Tsallis function describes the inelastic $y-$ and $p_{\mathrm{T}}-$binned spectra an additional correction to the number of events has to be taken into account. By scaling the number of events with the trigger efficiency of about (0.745 ± 0.019) for the detection of events with inelastic pp collisions, the true number of inelastic events N_{inel} for the normalisation is obtained [21]. Another contribution to the normalisation is the individual weighting of each p_{T} bin with the corresponding bin widths. The weighting factor due to the y width is equal to 1 because the spectra are at mid-rapidity $|y| < 0.5$. The final result of the corrected and normalized $p\mathrm{T}-$binned spectra at mid-rapidity $|y| < 0.5$ is shown in Fig. 3.13. The reason why the second bin of the spectrum shows a deviation from the shape of the function is subject of further investigations. The values for the free parameters are presented in Tab. 3.1 and were obtained by successive fitting of the function. The first fit was done for a p_{T} larger than $p_{\mathrm{T}} > 2.3$ GeV for the second fit the paramet-

Table 3.1: *Values with associated uncertainties for the free parameters determined from the Levi-Tsallis fit.*

dN	C (GeV)	n
(0.040 ± 0.017)	(0.40 ± 0.14)	(13 ± 8)

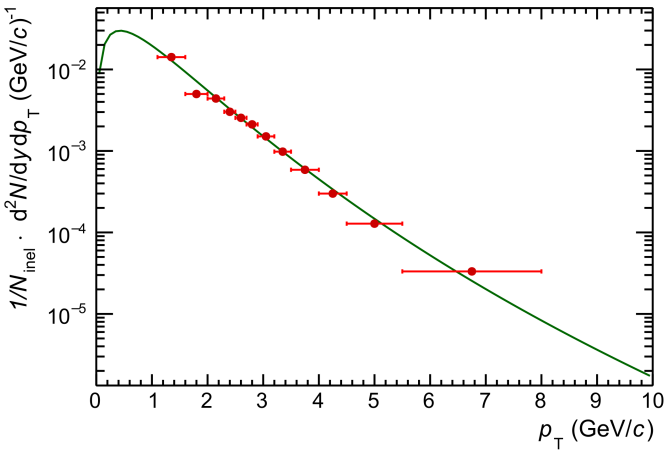

Figure 3.13: *Corrected and normalized yield of Σ^0 for the different y and p_{T} bins. Fitted with a Levi-Tsallis function (green).*

ers of the first were used as starting parameters and the fitting range was widened to encompass the whole range form 0 GeV up to 10 GeV. This fitting procedure was repeated with different starting ranges larger than $p_{\mathrm{T}} > 2.3$ GeV, however no significant change in the parameter values has been observed.

3.5 Determination of the ratio Σ^0/Λ

In order to make full use of the amount of reconstructed Σ^0 (Λ) the assertion an equal number of Σ^0 (Λ) and $\overline{\Sigma^0}$ ($\overline{\Lambda^0}$) are produced is made, from which follows:

$$\frac{\Sigma^0}{\Lambda} = \frac{(\Sigma^0 \oplus \overline{\Sigma^0})}{(\Lambda \oplus \overline{\Lambda})} \ . \tag{3.4}$$

The ratio of Σ^0 to Λ is determined by the ratio of their corresponding $y-$ and $p_{\mathrm{T}}-$binned spectra, shown in Fig. 3.14, with all corrections and normalisations applied. The result for the ratio as a function of p_{T} is shown in Fig. 3.14. For Λ the $p_{\mathrm{T}}-$binned spectrum of $(\Lambda \oplus \overline{\Lambda})$ was taken from [18]. The ratio varies for each p_{T}

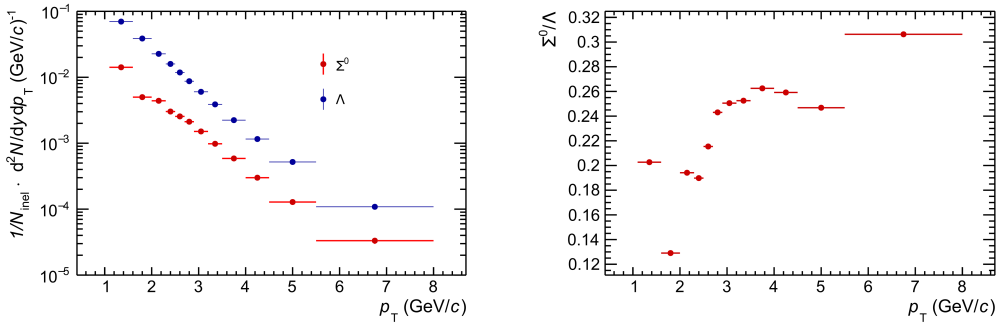

(a) (b)

Figure 3.14: *Normalized yields (a) of* Σ^0 *and* Λ *as a function of* p_{T}. *Ratio of* Σ^0 *to* Λ *(b) as a function of* p_{T}. *The spectra for* Λ *was taken from [18].*

bin and shows an upwards trend towards higher p_{T}, meaning more and more Σ^0 are seen. The reason why the second bin in each figure shows a deviation from the observed trend is subject of further investigations. The ratio for the extrapolated p_{T} spectrum is the result of ratio of the values for $\mathrm{d}N$, obtained by the Levi-Tsallis fit,

$$\frac{(\Sigma^0 \oplus \overline{\Sigma^0})}{(\Lambda \oplus \overline{\Lambda})} = \frac{\mathrm{d}N^{(\Sigma^0 \oplus \overline{\Sigma^0})}}{\mathrm{d}N^{(\Lambda \oplus \overline{\Lambda})}}. \tag{3.5}$$

The value for $\mathrm{d}N^{(\Lambda \oplus \overline{\Lambda})}$ was taken from [18]. The uncertainty of $\mathrm{d}N^{(\Sigma^0 \oplus \overline{\Sigma^0})}/\,\mathrm{d}N^{(\Lambda \oplus \overline{\Lambda})}$ was calculated by propagating the statistical uncertainty of $\mathrm{d}N^{(\Sigma^0 \oplus \overline{\Sigma^0})}$ and the combined uncertainty of $\mathrm{d}N^{(\Lambda \oplus \overline{\Lambda})}$. The result of (0.219 ± 0.005) is in the same order of magnitude as the expected theoretical value of $1/3$. The deviation of the obtained ratio from the value predicted by theory is subject of further investigation, including a detailed analysis of systematic uncertainties. This important result shows that there can be no significant deviations of the production mechanisms for Σ^0 with respect to mechanisms for Λ. Which means that the governing physics of the pp collision at lower $\sqrt{s}$, but above the production threshold of Σ^0, are at least similar to those at a collision energy of $\sqrt{s} = 13$ TeV. Furthermore it shows that the productions mechanisms, in pp collisions, at these energies are not strongly dependent on the isospin of the produced particle.

Chapter 4

Summary and outlook

For the analysis 1.04×10^9 min. bias pp events from 2016 and 2017 were used. First, the selection criteria for the photon reconstruction, were refined by carefully optimizing the cut parameters with the help of MC simulations. Then, the $p_{\mathrm{T}}-$integrated invariant mass spectrum of Σ^0 was successfully extracted from data. Which allowed the determination of the $p_{\mathrm{T}}-$integrated yield of (24989 ± 317) , which is about a factor of 2.5 larger than the yield observed with non-optimized cuts. Furthermore the mean and width of the signal were studied. In order to compare the yield of Σ^0 and Λ the $p_{\mathrm{T}}-$binned invariant mass spectra at mid-rapidity $|y| < 0.5$ have been obtained, for each the mean and width of the signal as well as the yield were determined. All measured means are in good agreement with the PDG [13] value for the mass of Σ^0. An comparison with the MC dataset showed good agreement. For the yield as a function of p_{T} the purity was calculated, from which the p_{T} averaged value was calculated to be 26.4 %. In the following, the yields have been corrected with $\varepsilon_{rec \times acc}$, derived from the associated MC production and normalized to the corrected number of inelastic pp collsions. Subsequently, a $p_{\mathrm{T}}-$binned ratio of Σ^0/Λ has been obtained. Finally an extrapolation of the yield for low ranges of $p_{\mathrm{T}} < 1.1$ GeV/c was generated by fitting a Levi-Tsallis function to the data. And the value of $\mathrm{d}N = (0.040 \pm 0.017)$, was extracted from the fit. With this value the ratio of Σ^0/Λ was calculated to be (0.219 ± 0.005), which is in the same order of magnitude as the theoretical prediction of 1/3. This is a direct hint that the production mechanisms are not strongly affected by the isospin. In conclusion, the goal of the analysis to increase the yield of Σ^0, by improving the PID for the photon, was successfully achieved, furthermore the calculated ratio of Σ^0/Λ showed no significant deviation from the theoretical prediction.

Looking forward, with the integration of new data sets from 2018 and eventually RUN3 data even more Σ^0 will be reconstructed with the optimized cuts. As of now the fine tuned selection criteria developed in this analysis were used for the Σ^0 reconstruction in high multiplicity pp events. The deviation of the obtained ratio for Σ^0/Λ from the value predicted by theory is subject of further investigation, including a detailed analysis of systematic uncertainties.

Bibliography

[1] S.Bethke, Experimental tests of asymptotic freedom, journal: Prog. in Part. and Nuc. Phys., year 2007, p.351-386.

[2] B. Müller, Investigation of Hot QCD Matter: Theoretical Aspects, journal: Phys. Scripta, year 2013, p.1, url: https://arxiv.org/abs/1309.7616.

[3] Johann Rafelski and Berndt Mueller, Strangeness production in the quark-gluon plasma, publisher: American Physical Society, journal: Physical Review Letters, year 1982, p.16, url: https://www.researchgate.net/publication/283173575-Strangeness-production-in-the-Quark-Gluon-plasma.

[4] The ALICE Collaboration, Enhanced production of multi-strange hadrons in high-multiplicity proton-proton collisions, journal: Nature Phys., year 2017, p.535-539, url: https://arxiv.org/abs/1606.07424.

[5] Trassiorf, Baryon-octet, year 2007, url: https://commons.wikimedia.org/wiki/File:Baryon-octet.svg.

[6] The ALICE Collaboration, analysis-note: Σ^0 and $\overline{\Sigma^0}$ Baryon Production in pp Collisions at $\sqrt(s)$=7 TeV from the Analysis of 2010 Pass-4 ALICE Data, year 2017, url: https://alice-notes.web.cern.ch/node/562.

[7] Lonardoni, Diego and Lovato, Alessandro and Gandolfi, Stefano and Pederiva, Francesco, Hyperon Puzzle: Hints from Quantum Monte Carlo Calculations, journal: Phys. Rev. Lett., year 2015, p.5, url: https://link.aps.org/doi/10.1103/PhysRevLett.114.092301.

[8] Gene Van Buren for the STAR Collaboration, The Ratio Sigma0/Lambda at RHIC, year 2005, url: https://arxiv.org/abs/nucl-ex/0512018.

[9] E. Botta for the ALICE Collaboration, Particle identification performance at ALICE, year 2017, p.1-2, url: https://arxiv.org/abs/1709.00288.

[10] The ALICE Collaboration, The ALICE experiment at the CERN LHC, publisher: Institute of Physics Publishing and SISSA, year 2008, p. 3/8/13/55/56, url: https://arxiv.org/abs/1402.4476.

[11] The ALICE Collaboration, year 2018, url: https://alice-figure.web.cern.ch/node/8670.

[12] A. Akindinov et al., Performance of the ALICE Time-Of-Flight detector at the LHC, journal: Phys. Rev. D, year 2013, p.1, url: http://inspirehep.net/record/1231795?ln=de.

[13] M. Tanabashi, journal: Eur. Phys. J. Plus, year 2018, url: http://pdg.lbl.gov/2018/listings/rpp2018-list-sigma-zero.pdf.

[14] M. Tanabashi, journal: Phys. Rev. D, year 2018, url: http://pdg.lbl.gov/2018/listings/rpp2018-list-lambda.pdf.

[15] The ALICE Collaboration, analysis-note: $\Sigma^0(1192)$ signal extraction in pp collisions at $\sqrt(s)$=7 TeV (QM2014), year 2014, url: https://alice-figure.web.cern.ch/node/6407.

[16] The ALICE Collaboration, analysis-note: Material determination with conversions in ALICE in proton-proton collisions at $\sqrt(s) = 7$ TeV at the CERN LHC, year 2012, p.3/12, url: https://alice-notes.web.cern.ch/node/51.

[17] T. Dahms, Measurement of photons via conversion pairs with the PHENIX experiment at RHIC, year 2005, url: http://www.phenix.bnl.gov/phenix/WWW/publish/tdahms/master-thesis/tdahms-thesis.pdf.

[18] The ALICE Collaboration, K^0_S, Λ and $\bar{\Lambda}$ production in proton–proton collisions at $\sqrt{s}$ = 13 TeV, year 2017, url: https://alice-notes.web.cern.ch/system/files/notes/analysis/425/2017-Jan-16-analysis-note-V0s-in-minbias-pp13TeV-v5.pdf.

[19] T.Sjöstrand et al., An Introduction to PYTHIA 8.2, journal: Comput. Phys. Commun., year 2015, p.159-177, url: https://arxiv.org/abs/1410.3012.

[20] T.Sjöstrand et al., PYTHIA 6.4 Physics and Manual, journal: JHEP, year 2006, p.26, url: https://arxiv.org/abs/hep-ph/0603175.

[21] The ALICE Collaboration, ALICE luminosity determination for pp collisions at $\sqrt{s} = 13$ TeV, year 2016, url: https://cds.cern.ch/record/2160174.

Acknowledgements

This work would not have been possible without the help of the great many people surrounding me. At first, I would like to express my gratitude to Prof. Laura Fabbietti for giving me chance to work on this fascinating topic, her encouragement to participate in the "Bergamo Days" or in the FSP meeting and kindness. Secondly I am most thankful to my supervisor Andreas Mathis, his constant support, enthusiasm for analyses and cheerfulness amazed me. Further I would like to thank all the other members of chair E12, who I had the pleasure to work with and/or shared my office. The atmosphere and overall spirit in the group made me feel very comfortable since the day I stated to work on this thesis. Finally I wish to thank the people dear to me and supported me throughout my live, my family and my girlfriend.